ACS APPLIED MATERIALS & INTERFACES

www.acsami.org

Research Article

In Situ Formation of Au-Glycopolymer Nanoparticles for Surface-Enhanced Raman Scattering-Based Biosensing and Single-Cell Immunity

Zi-Chun Chia,[⊥] Li-Xing Yang,[⊥] Ting-Yu Cheng, Ya-Jyun Chen, Horng-Long Cheng, Fei-Ting Hsu, Ying-Jan Wang, Yu-Ying Chen, Tzu-Chi Huang, Yi-Syun Fang, and Chih-Chia Huang*

Cite This: *ACS Appl. Mater. Interfaces* 2021, 13, 52295−52307

Read Online

ACCESS | Metrics & More | Article Recommendations | Supporting Information

ABSTRACT: Successful synthesis of glyconanoparticles has attracted much attention due to their various biointeractive capabilities, but it is still a challenge to understand different single-cell responses to exogenous particles among cell populations. Herein, we designed polyaniline-containing galactosylated gold nanoparticles (Au@PGlyco NPs) via in situ polymerization of ortho-nitrophenyl-β-galactoside assisted by Au nucleation. The nanogold-carrying polyaniline block produced electromagnetic enhancement in surface-enhanced Raman scattering (SERS). The underlying polymerization mechanism of ortho-nitrophenyl compounds via the formation of Au nanoparticles was investigated. Depending on how the galactoside moiety reacted with β-galactosidase derived from bacteria, the Au@PGlyco NPs-mediated SERS biosensor could detect low amounts of bacteria (~1 × 10^2 CFU/mL). In addition, a high accumulation of Au@PGlyco NPs mediated the immune response of tumor-associated M2 macrophages to the immunogenic M1 macrophage transition, which was elicited by reactive oxygen levels biostimulation using single-cell SERS-combined fluorescence imaging. Our study suggested that Au@PGlyco NPs may serve as a biosensing platform with the labeling capacity on galactose-binding receptors expressed cell and immune regulation.

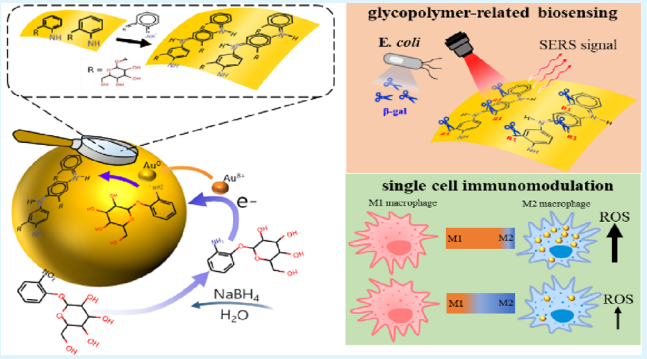

KEYWORDS: *glycopolymer gold nanoparticles, surface-enhanced Raman scattering, biosensing, single-cell detection, macrophage polarization*

1. INTRODUCTION

Carbohydrates play an essential role in a diverse array of biological activities, including molecular recognition, cell adhesion, metabolism, and immune responses.[1−3] Due to the functionality of carbohydrates, glycopolymer-based nanoparticles are emerging as novel materials that enable well-defined structures with high affinities and biocompatibilities due to the multivalent binding between glycans and proteins, providing attractive materials for applications in immune regulation,[4] vaccines,[5] targeted delivery,[6,7] infection treatment,[8,9] and biosensing.[10,11] Recently, Jain *et al.* reviewed the possible development of galactosylated nanoparticles for active delivery to tumors by modern sensing of bio-targeting lectin receptors (e.g., glycoprotein receptor in hepatocellular carcinoma, C-type lectin receptor in dendritic cells, macrophages, and tumor cells, and galactose lectin receptor in cancer cells)[6] or active transport to the glucose/galactose binding proteins of *Escherichia coli* (E. *coli*).[12] In addition to the utility of glycosides for improving targeting capacity, there has been emerging interest in the development of galactose terminal nanoparticles to facilitate the efficacy of checkpoint inhibitor-based immunotherapy by repolarizing macrophages of tumor-associated macrophages (M2) into the proinflammatory (M1) type.[13−15] Although it has been found that the exposure of greater galactose moieties showed greater advantages in promoting the shift of the macrophage transition,[14,16] the correlation between galactosylated material accumulation and macrophage reprogramming has not been elucidated. Therefore, smart optical carrier development with a less invasive approach is required for a better understanding of the dynamic in carbohydrate-related biological processes, including targeting, internalization, and endogenous stimuli−response.

Received: July 19, 2021
Accepted: October 19, 2021
Published: October 27, 2021

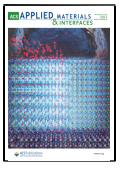

https://doi.org/10.1021/acsami.1c13647
ACS Appl. Mater. Interfaces 2021, 13, 52295−52307

Scheme 1. Possible Formation Pathway of the Au@PGlyco NPs by an Interfacial Catalysis-Assisted Reduction of the Nitro Moiety at ONPG Followed by 1,4-Coupling Polymerization through the Capture of the Anilino Radical from the Oxidation of 2-Aminophenyl β-D-galactopyranoside with Au Ions at the Au Seed Interface[a]

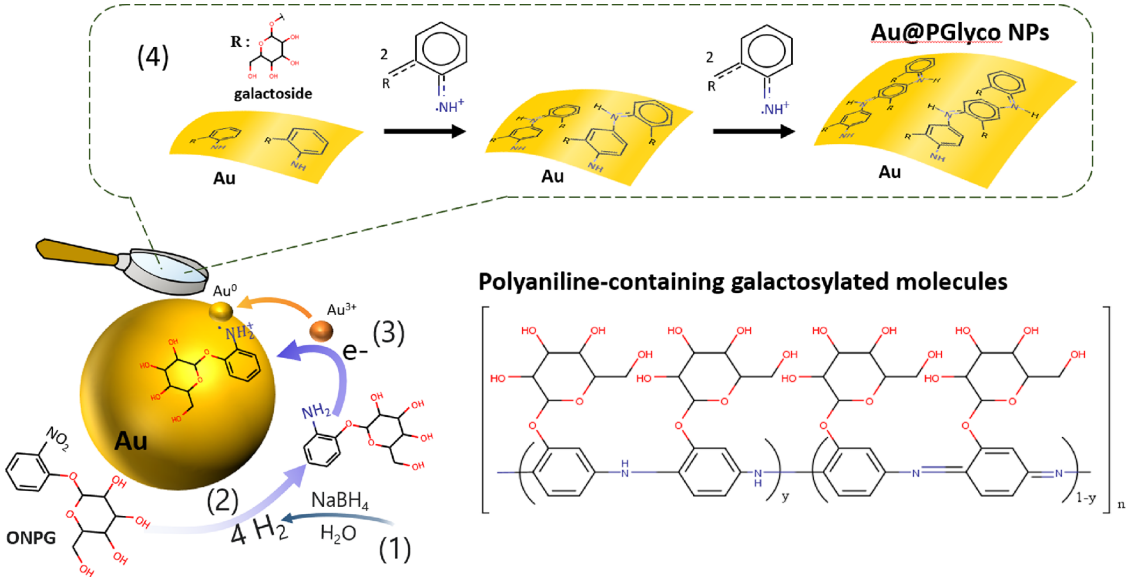

[a]The polyaniline-containing galactosylated molecules are constructed on the surface of the Au NPs.

In general, glycopolymer-based nanoparticles can promote endocytosis of cellular internalization and endow a more potent multivalent effect,[3,14−16] and it can be designed through two methods: polymerization with carbohydrate-functionalized monomers and implantation of carbohydrates onto a polymer backbone through thiol ligand (Au−S) binding.[17] The conjugation methods for linking saccharide chains include the ring opening of hexose to expose the free aldehyde group followed by reaction with amino groups at the nanocarrier,[18] esterification of galactose to link alkynyl to an azido-functional polymer,[19] and chemical substitution at the C2 and C5-pyranose positions.[20] However, the synthesis of sugar-coated and glycopolymer-bioconjugated gold nanoparticles requires complex preparation and additional post-modification,[21,22] which usually denature the ligands and affect the functionality. An example of such modification includes the oxidation of the C-6-OH positions in saccharides.[8,23,24]

Herein, we developed a facile core−shell polymerization process to fabricate homomultivalent galactose-functionalized Au nanoparticles by simultaneous hybridization of ortho-nitrophenyl-β-galactoside (ONPG) and nucleation growth of Au seeds (Scheme 1). In situ Raman measurements demonstrated the rapid evolution of surface-enhanced Raman scattering (SERS) signals from the formation of a polyaniline (PANI)-structured backbone chain after the reduction of $HAuCl_4$ by $NaBH_4$ based on the SERS signal amplification by plasmonic Au NPs.[25−28] The primary interfacial polymerization was universal for extending the fabrication of other Au core-coating PANI-based shell NPs. The PANI-containing galactose pendants are SERS-active glycopolymers in close proximity to the Au nanoparticle surface (Au@PGlyco NPs). Apart from the label-free method that is susceptible to foreign signals[29−32] and the labeling SERS-tags method that requires additional synthesis techniques for modifying specific reporters or ligands,[28,33−35] we designed a SERS-active glycopolymer on Au NPs that could respond to the galactose-related enzyme and cellular receptors. Considering the SERS-active glycopolymer coating, this new design of Au@PGlyco NPs for bio-SERS sensing and non-invasive micro-SERS technology[28,31−33] could directly monitor galactose-targeted reaction with SERS response in two typical biological platforms: (1) the negative signal change of Au@PGlyco NPs for a bio-SERS response to β-gal, acting as a sensitive bacterial sensor at 100 CFU/mL *E. coli* and (2) the concentration-dependent galactose-based positive SERS response of single-cell analysis for investigating the macrophage model through the galactose-binding receptor binding effect, which could improve cell endocytosis and simultaneously enhance reactive oxygen species (ROS) levels[36] in cells and thus increase the transition of macrophages from M2 to M1.

2. RESULTS AND DISCUSSION

Figure 1a shows a transmission electron microscopy (TEM) image of the prepared Au@PGlyco NPs with polyhedral structures, including pentagon, hexagon, sphere, and triangle shapes. The average diameter of these particles was estimated to be 18.1 ± 5.7 nm from the dark contrast area in the TEM image, and the particles consisted of a face-centered cubic (fcc) Au crystal structure (Figure S1). The hydrodynamic diameter is 33.4 ± 8.0 nm with a polydispersity index (PDI) of 0.057, showing high dispersity of colloids in water (Figure S2).[37] The larger particle diameter by dynamic light scattering (DLS)[37,38] compared with TEM size analysis was expected due to the increase in the additional thickness of the water-swellable organic capping layer[14,22,24] around the surface of a solid Au nanoparticle (~18.1 nm) in water. The coating of glycan-based macromolecule was validated by element- and structure-analysis instruments as described below. By high-magnification TEM imaging (Figure 1b-i), obvious light contrast (~2.6 nm) surrounding the solid counterpart of the nanogold was obtained with respect to the coating of organic composites due to the mere addition of ONPG molecules during the synthesis. The high-resolution TEM (HR-TEM) shown in Figure 1c presents the highly crystalline structure of the

https://doi.org/10.1021/acsami.1c13647
ACS Appl. Mater. Interfaces 2021, 13, 52295−52307

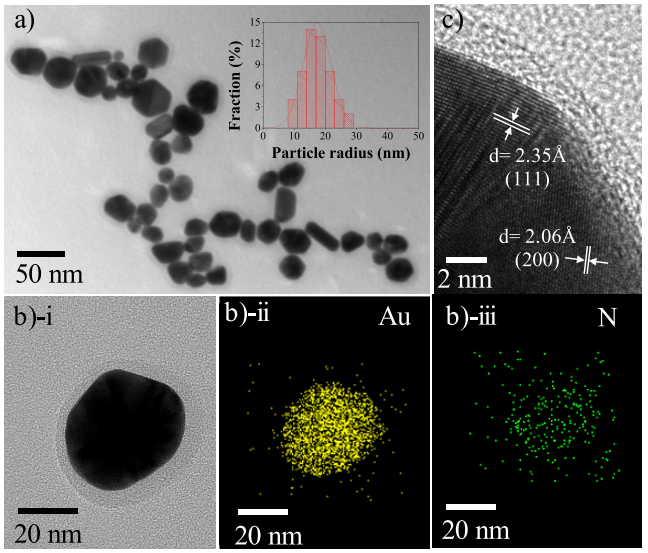

Figure 1. (a) TEM image, (b-i) high-magnification TEM image, and (c) HR-TEM image of Au@PGlyco NPs. Inset in (a): particle diameter distribution by TEM image. Corresponding EDS mapping images of (b-ii) Au and (b-iii) N in a single particle.

periodic pattern of d_1 (2.35 Å), and d_2 (2.09 Å) corresponds to the $(111)_{Au}$ and $(200)_{Au}$ planes. EDS mapping measurements (Figure 1b-ii,b-iii) determined that trace amounts of N were distributed on the surface and main body of the Au@PGlyco NPs; these N atoms originated from the conjugation of nitrogen to the galactoside moiety. The additional TGA measurement of the Au@PGlyco NPs determined ~5.28% of weight loss for the organic galactoside deposition (Figure S3a).

The FT-IR spectra of ONPG powder and Au@PGlyco NPs prepared using different concentrations of ONPG are shown in Figure 2a. The relatively strong signals at 3400, 1035, and 1066 cm^{-1} in the FT-IR spectra of Au@PGlyco NPs were attributed to the −OH stretching, C−O stretching, and C−OH bending from the galactose structure, respectively.[39] The binding energy of C 1s appeared at 286.5 eV, which was assigned to the sugar-based fingerprints of the C−O−C and C−OH structures[40] based on X-ray photoelectron spectroscopy (XPS) (Figure S3b). Notably, the intensities of specific peaks at 1525 cm^{-1} (ν_{asym}) and 1378 cm^{-1} (ν_{sym}), which were attributed to the NO_2 group,[41] were dramatically decreased upon the formation of the Au@PGlyco NPs (Figure 2a). To understand the organic structure from the conversion of the ONPG precursor after reaction, we performed Raman spectroscopy to explore the molecular structure of Au@PGlyco NPs. Figure 2b shows the great enhancement of the Au@PGlyco NPs bands at 1159, 1232, 1314, 1343, 1423−1507, and 1590−1627 cm^{-1}, which did not match the characteristic Raman bands of ONPG powder, galactose powder, or galactose-coated (Au@GA) NPs (Figure S4a). The highly enhanced Raman signals of the Au@PGlyco NPs originated from the well-known SERS mechanism that promotes strong coupling with the electromagnetic field by nanogold through molecular adsorption due to proximity.[28,29,42,43] The SERS enhancement is induced at 633−671 nm (Figure S5a−d). The evolved SERS signal is a function of laser power by using 671 nm laser as a model (Figure S5a−c). Noted that the corresponding SERS evolution matched with the surface plasmon resonance of Au@PGlyco NPs at 633−

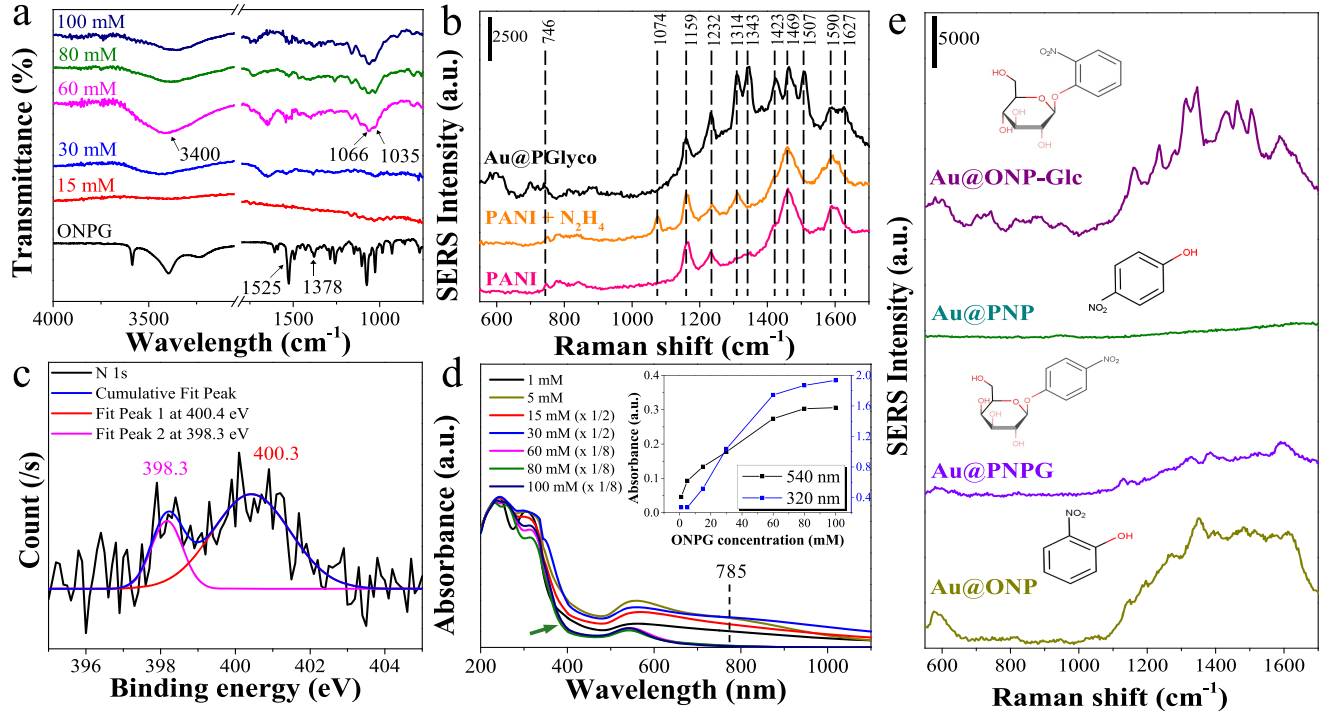

Figure 2. (a) FT-IR spectra of the ONPG molecule and Au@PGlyco NPs prepared with 15, 30, 60, 80, and 100 mM ONPG. (b) SERS spectrum of Au@PGlyco NPs, PANI powder, and PANI+N_2H_4. (c) N 1s orbital XPS spectrum of $Au@PGlyco_{[80\ mM\ ONPG]}$ NPs. (d) Absorption spectra of Au@PGlyco NPs prepared using 1−100 mM ONPG molecules (without sample purification). The green arrow indicates the $Au@PGlyco_{[80\ mM\ ONPG]}$ NPs, and the dashed line label indicates the laser light position at 785 nm. Inset: plot of absorbance at 320 nm (blue line) and 540 nm (black line) versus ONPG concentrations. (e) SERS spectrum of Au-based NPs synthesized using ONP, PNPG, PNP, and ONP-Glc molecules.

https://doi.org/10.1021/acsami.1c13647
ACS Appl. Mater. Interfaces 2021, 13, 52295−52307

671 nm (Figure S5d,e),[43] and responded to the relative low SERS performance by low absorbance of Au@PGlyco NPs at 785 nm (labeled by a green arrow and dashed line in Figure 2d), which may be related to the far-field effect by the electromagnetic field of nanogold.[29,30,43,44] The inferior SERS performance at 785 nm is also affected by longer wavelength excitation photons based on the Raman intensity proportional to the fourth power of laser excitation frequency (ν^4).[42] The SERS signal intensity of the Au@PGlyco NPs is linearly related to the sample concentrations (Figure S5e−h), indicating the offered SERS due to the dispersed Au NPs (Figure S5i) rather than the appearance of boost SERS generation as high as 10−100[28,42,45] orders of magnitude by aggregation-related hot spots.

Both DFT-optimized Raman calculations (Figure S4b) and experimental results (Figure S4c and Video S1) indicated the low and inconsistent SERS response from the close attachment between the Au core and ONPG molecules when compared with the Au@PGlyco NPs-mediated SERS of the black curve in Figure 2b. Intriguingly, these microstructured peaks due to the Au@PGlyco NPs are similar to the vibrational structure profiles of PANI peaks (Figure 2b). Therefore, we tentatively determined the assignments of the Raman shift peaks: the peak at 1627 cm^{-1} corresponds to the C−C stretching of a benzenoid ring, 1590 cm^{-1} corresponds to the C═C stretching of a quinonoid ring, 1507 cm^{-1} corresponds to the N−H bending, 1469 cm^{-1} corresponds to the C═N stretching of a quinonoid ring, 1343−1314 cm^{-1} corresponds to the C−N stretching of a secondary aromatic amine, 1232 cm^{-1} corresponds to the C−N stretching of a benzenoid ring, 1159 cm^{-1} corresponds to the C−H in-plane bending of a quinonoid ring, and 746 cm^{-1} corresponds to the quinonoid ring bending.[46−48] A slight shift at 1−7 cm^{-1} indicates a shift in the quinonoid/benzenoid structure of the Au@PGlyco NPs in contrast to the pure PANI, and it is attributed to the different chemical environment in which galactose is linked to the PANI backbone and the condensed PANI-based glycopolymers have strong hydrogen bonds. In Figure 2c, the N 1s orbital of the Au@PGlyco NPs appeared at a binding energy of 398.3 eV, which could be assigned to the quinonoid imine (═N−). A broadened band at ∼400 eV was related to the overlapping benzenoid amine (−N−) and protonated benzenoid amine ($-N^{+}H-$) structures of polyaniline.[49] The higher binding energy of the N 1s orbital at 401.1−402.6 eV corresponds to N═O bonds that did not arise in spectrum.[40,50] The UV−visible spectra in Figure 2d show the appearance of a broadening absorption profile at 1−30 mM ONPG, which could be attributed to the generation of colloidal Au with irregular and more aggregated particle structures (Figure S6a−d). The typical absorption band was altered to the focused single band and reached a plateau when ONPG concentrations of 60−100 mM were added. At least 60 mM ONPG was necessary to produce free-standing particles (Figure S6e).

Figure S7 shows that the overall SERS signal intensity of Au@PGlyco NPs decreased as the ONPG concentration decreased to 15 mM. The benzenoid ring-related Raman peaks at 1627, 1507, 1343, and 1232 cm^{-1} were the dominant signals, which were related to the preferred adsorbed orientation by the benzenoid ring and secondary amine of PANI instead of the imine links. We performed Raman spectroscopy to monitor the reaction of pure PANI powder with a hydrazine reductant (Figure 2b), and the subsequent increase in the peak intensity at 1314 cm^{-1} was in agreement with the relationship of the strong band at 1314 cm^{-1} with the increasing fraction of a secondary aromatic amine (reduction form) from PANI.

To investigate the formation mechanism of the Au@PGlyco NPs, we set up in situ Raman measurements to monitor the synthesis and evolution of the glycopolymer (Figure Sa). Figure S8b and Video S2 show the reaction observation for the immediate generation of the dark-red Au colloid after the addition of $NaBH_4$ followed by rapid evolution of PANI-based Raman peaks ∼0.5 s post-injection. According to the DFT simulation, the intramolecular distance between the R-NO_2 of the ONPG molecule and the Au atom is shorter (0.234−0.236 nm) than the distance between the galactoside moiety and the Au atom (Figure S4b). The electron flow through the Au atom facilitates the reduction of the nitro group at ONPG upon the dissociation of the $NaBH_4$ molecule. Hence, we presumed that the initial reaction involved the conversion of the nitro group of ONPG into 2-aminophenyl β-D-galactopyranoside (AMPG) by the Au interfacial catalyst-assisted reduction mechanism,[29,51] as illustrated in (1) and (2) in Scheme 1. Figure 2d shows that the yield of Au NPs increased with an increasing load of ONPG molecules, indicating additional electron donation to the Au ions by the oxidation of adsorbed AMPG (Scheme 1, (3)). We ruled out the reduction of the Au ions from the oxidation of galactose and nitro groups of ONPG molecules at 80 °C (Figure S9). Finally, such oxidation of AMPG subsequently initiated the polymerization process to form a glycopolymer that was decorated on the surface of the Au nanocatalyst (Scheme 1, (4)). Similar oxidation-assisted polymerization of the aniline and aniline derivatives has been explored in the presence of Cu ions[52] and Ag ions.[53] Regarding the above potential reaction with Au and Cu ions, further investigation on Ag and Cu nucleation to synthesize other metal@PGlyco NPs with composite-, size-, and shape-dependent SERS manners is ongoing and will be reported in our follow-up paper.

Furthermore, to gain a deeper understanding of the glycopolymer formation mechanism, we utilized 4-nitrophenyl β-D-glucopyranoside (ONP-Glc) with substituents at the 1,4-positions of benzene by galactose and nitro groups to fabricate Au@ONP-Glc NPs. Figure 2e presents the noise-like SERS signals that appear after the formation of Au NPs. Likewise, we investigated the in situ polymerization reaction with ortho-nitrophenol (ONP) under the same synthesis conditions as the Au NPs. The primary peaks expressed at 1627, 1343, and 1159 cm^{-1} were obtained (Figure 2e). In contrast, a vanishing optical signal appears in the SERS spectrum when ONP is replaced with *para*-nitrophenol (PNP) in the same colloidal synthesis, which is related to the obstruction in the linkage through 1,4 *para*-coupling benzene of the galactoside. In fact, the same in situ hybridization could successfully fabricate other PANI-based Au@glycopolymer NPs (i.e., polyglucosylated Au nanoparticles from 2-nitrophenyl beta-D-glucopyranoside) (Figure 2e), and this Au-catalyzed polymerization did not occur when the nitro group was absent in phenyl-*b*-D-galactopyranoside (Figure S10a) and when there was a lack of ortho-nitrophyl groups in the methyl-*b*-D-galactopyranoside (Figure S10b) and galactose alone (Figure S10c).

There are several advantages of utility of Au@PGlyco NPs. First, 20 synthetic batches of as-prepared Au@PGlyco NPs with a small relative standard deviation at 8.94% were obtained, indicating the good reproducible signals by the independent synthesis (Figure S11). Second, Au@PGlyco NPs could directly possess SERS signals by the PANI backbone on

https://doi.org/10.1021/acsami.1c13647
ACS Appl. Mater. Interfaces 2021, 13, 52295−52307

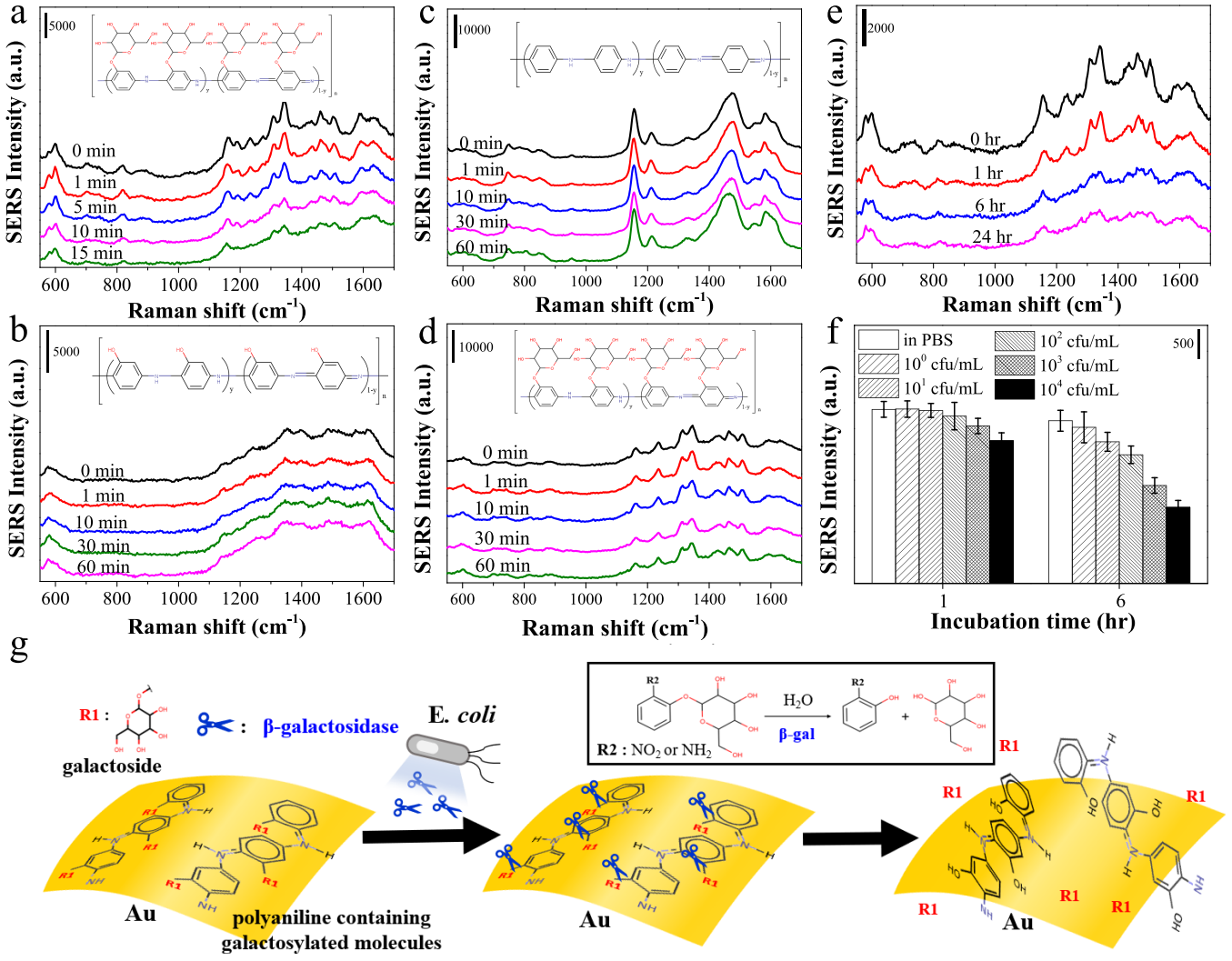

Figure 3. SERS spectra of (a) Au@PGlyco, (b) Au@ONP, (c) Au@PANI, and (d) Au@ONP-Glc NPs reacted with 20 μM β-gal within 60 min (inset: the proposed molecular structure based on the synthesis of Au NPs with ONPG, ONP, PANI, and ONP-Glc, respectively). (e) SERS spectra of Au@ONPG solution mixed with 1×10^4 CFU/mL *E. coli* within 24 h of incubation. (f) Relationship between the SERS intensity at 1159 cm^{-1} and the bacterial preincubation time in PBS solution. (g) Scheme for the possible reaction of Au@PGlyco NPs with β-gal. The molecular structures in the insets of (a)−(d) illustrate the proposed configuration of the corresponding polyaniline derivatives.

the Au surface[43,54] and offer homomultivalent targeting capability by a galactose-rich surface without the post-immobilized SERS probes and capping layer protection that were reported in the previous works.[28,33−35] The enhancement factor (EF) of Au@PGlyco NPs that contained 5.28% of glycopolymer is 1.50×10^4 compared with the normal Raman characteristic peak at 1159 cm^{-1} of pure PANI (Figure S12a). Third, as shown in Figure S13, the Au@PGlyco NPs solution could produce consistent SERS intensity after 24 h of incubation in culture media (i.e., PBS, McCoy's 5a, RPMI, and DMEM) as well as in 0.1 mM H_2O_2 solution, which is the concentration level of endogenous H_2O_2 in the cytoplasm of cancer cells.[55,56] The robust SERS-active glycopolymer with a high EF results in the promising development of traceable biosensors for the subsequent molecular detection. Finally, the Au@PGlyco NPs detection toward a malachite green (MG) molecule could be lower to a nanomolar range at 671 nm excitation with an analytical EF (AEF) of 4.47×10^4 (Figure S12b,c), which is larger than and/or comparable with the results that used free-standing Au@Ag@polymer NPs,[26] Ag nano-octahedral single particles,[57] Au@PANI nanomaterials,[43] and Au nanorods[58] to be additionally used to sense small molecules. This AEF value of 4.47×10^4 is still insufficient to reach high sensitivity detection as reported in the literature because there are no hotspots induced by the aggregate state[28,42,59] and nanogap formation.[25]

2.1. SERS Sensing for Bacteria with Au@PGlyco NPs.

To evaluate the biological activity of the galactoside moiety at Au@PGlyco NPs, the enzymatic reaction with Au@PGlyco NPs was performed by reacting with 20 μM β-gal at room temperature for 60 min using a 671 nm Raman system. The presence of β-gal exhibited an observable decrease in the SERS intensity over a period of incubation time, indicating the enzyme reactivity of Au@PGlyco NPs triggered by β-gal (Figure 3a). The limit of detection (LOD) of detectable concentrations from 10^{-7} to 10^{-12} M β-gal in Figure S14 is 1.84×10^{-12} M calculated using 3σ/slope, where σ is the standard deviation of control samples and the slope is the linearity constant. As shown in Figure 3b,c, the SERS intensities of galactoside moiety-free Au@ONP and Au@PANI NPs did not vary within 60 min of incubation with β-gal. Likewise, the Au@ONP-Glc NPs possessed invariable SERS

https://doi.org/10.1021/acsami.1c13647
ACS Appl. Mater. Interfaces 2021, 13, 52295−52307

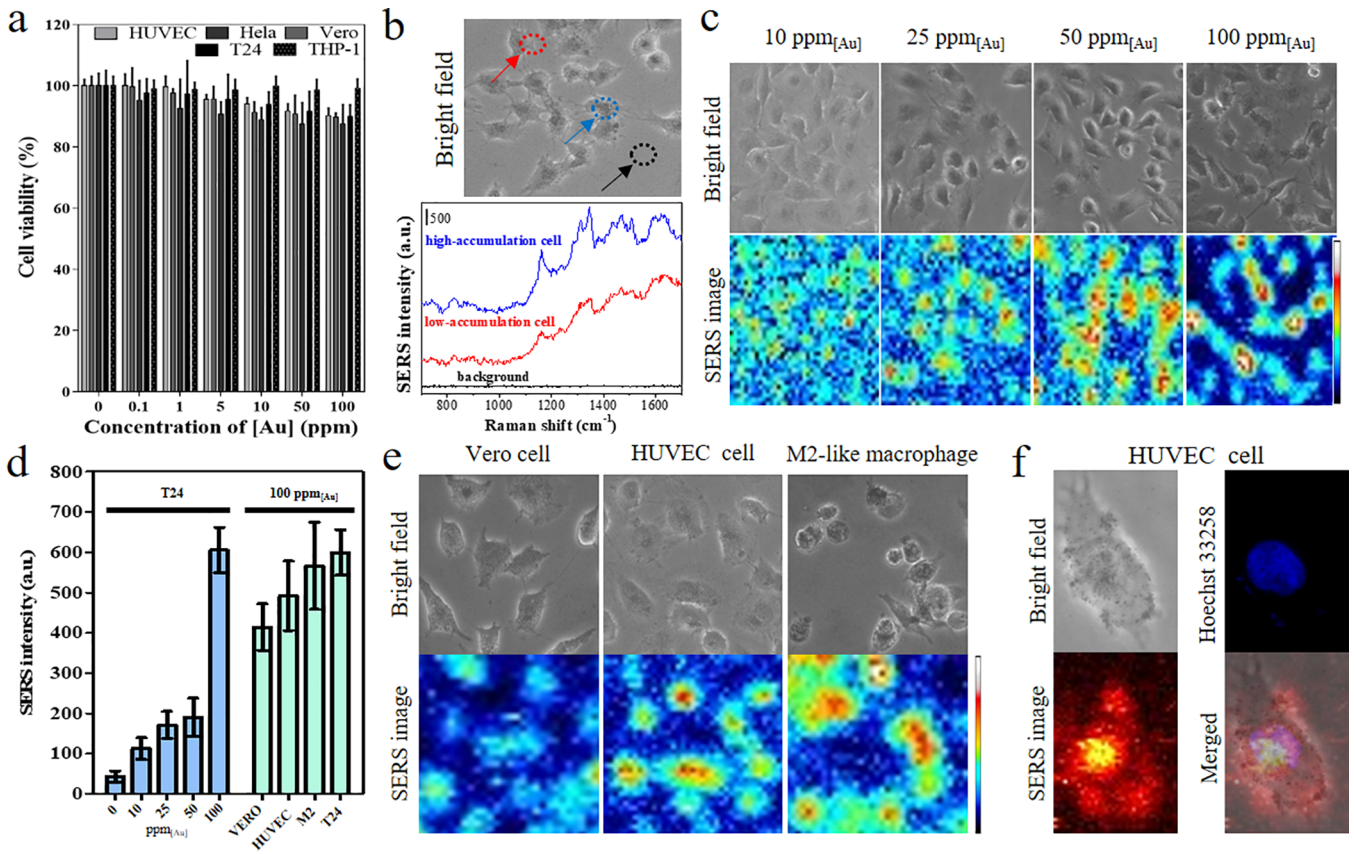

Figure 4. (a) Cell viability of Au@PGlyco NPs. (b) Bright-field image and SERS spectra of Au@PGlyco NPs-treated T24 cells. The line color represents the SERS signal corresponding to the same circle color area in (b). (c) Correlation of the intensity of the SERS signal with different concentrations of Au@PGlyco NPs in T24 cells. (d) The quantitation of the SERS signals in (c) is represented as a blue column, and the SERS signals from different cell types treated with 100 ppm Au@PGlyco NPs in (e) are represented as green columns. (e) SERS imaging in different cells with different intracellular localizations after 100 ppm Au@PGlyco NPs treatment. (f) Co-localization of SERS imaging and fluorescence microscopy imaging with nuclear staining in HUVECs treated with 100 ppm Au@PGlyco NPs.

intensity during the same enzymatic reaction due to exposure to the inactive glucose group (Figure 3d).

The intensity change of the SERS peaks of the Au@PGlyco NPs is considered to be due to the dissociation of the polyaniline backbone at the interface during the hydrolysis reaction triggered by β-gal (Figure 3g). A similar SERS intensity decline was demonstrated by breaking the hydrogen bonds after heating Au@PGlyco NPs (Figure S15), which is associated with the decrease in the intermolecular interaction between each SERS-active glycopolymer and weaken their cross-linking adsorption onto the plasmonic Au NPs. Both results elaborate that the SERS enhancement strongly relied on the surface effect. Specifically, the multiplex nitrogen atoms at the polyaniline-containing galactosylated molecule could bind to the plasmonic Au NP's surface,[54] which is an on-demand electromagnetic and chemical mechanism to exhibit strong SERS efficiency.[28,33,42]

In fact, β-gal is an essential enzyme that induces the lactose transport and metabolism system of *E. coli* bacteria, which can catalyze the hydrolysis of the galactoside moiety into monosaccharide units.[60] In Figure 3e, Au@PGlyco NPs were mixed with 10^4 CFU/mL *E. coli* bacteria for 1 h of incubation. The SERS signal change of the Au@PGlyco NPs shown in Figure 3e was a response to the β-gal activity originating from living *E. coli* bacteria due to the lack of noteworthy toxicity of the Au@PGlyco NPs (Figure S16). The SERS intensity was measured as the Au@PGlyco NPs reacted with *E. coli* bacteria ranging from 10^4 to 10^1 CFU/mL, as shown in Figure 3f and Figure S17. Compared with 1 h of incubation between the bacteria and Au@PGlyco NPs, 6 h of incubation released enough β-gal to improve the SERS signal change rate, allowing reliable detection of at least 1×10^2 CFU/mL. This SERS strategy based on the cluster-glycoside effect[61] and surface sensing mechanism is superior to the traditional colorimetric assay, which uses an ONPG indicator using a UV−vis spectrometer and has an LOD of 10^7−10^8 CFU/mL (Figure S18). The results were also superior to those of Nugen *et al.*, who designed enzyme-induced metallization colorimetric assays that had LOD values of 1×10^5 CFU/mL when gold nanorods were used and 1×10^4 CFU/mL when bacteriophage-conjugated magnetic probes were used.[62,63]

2.2. Au@PGlyco NPs-Mediated SERS Sensing and Immune Regulation in Mammalian Cells. Figure 4a indicates that Au@PGlyco NPs exhibited almost no cytotoxicity (viability >86% at 100 ppm$_{[Au]}$) to various cell lines, including T24, Vero, HUVECs, and M2-polarized THP-1 cells after 24 h of treatment with the 3-(4,5-dimethylthiazol-2-yl)-2,5-diphenyltetrazolium bromide (MTT) assay. The Au@PGlyco NPs might have a low cytotoxicity because the nanogold with the glycopolymer coating is bioinert. Inspired by the successful cellular detection of 10−20 nm Au NPs from the SERS image in microscopy,[31,32] next, we used micro-SERS-based analysis to evaluate the cellular uptake and distribution of Au@PGlyco NPs in mammalian cells. Figure 4b shows an

https://doi.org/10.1021/acsami.1c13647
ACS Appl. Mater. Interfaces 2021, 13, 52295−52307

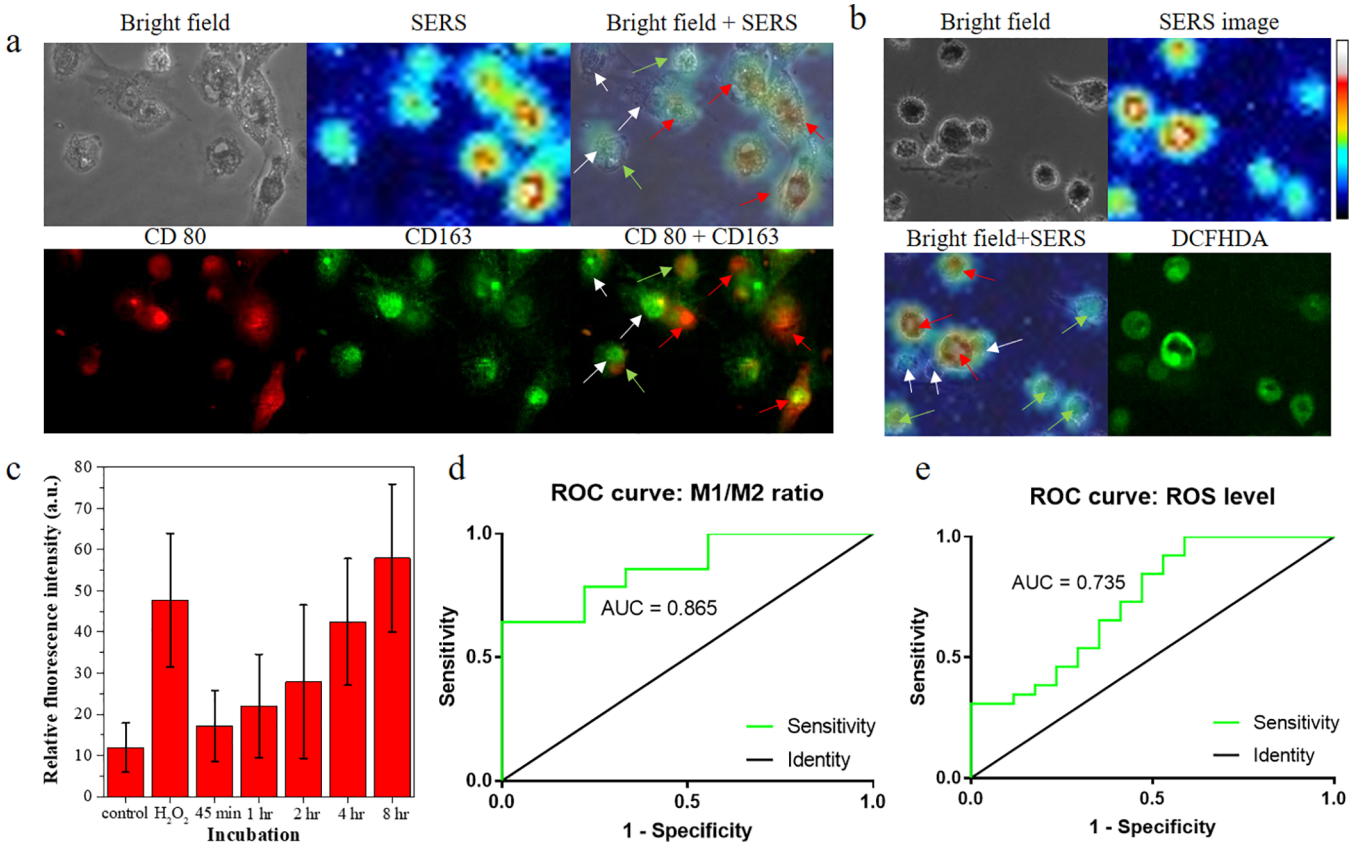

Figure 5. (a) Surface marker transition of M2 macrophages treated with 100 ppm Au@PGlyco NPs by SERS imaging and fluorescence microscopy imaging with CD80/CD163 labeling for single-cell analysis with M1 polarization status assessments. The correlation of SERS intensity and fluorescence intensity changes of the CD80 and CD163 is indicated by different color arrows. Red arrows represent a high SERS signal and high CD80/low CD163 cells, green arrows represent a low SERS signal and low CD80/high CD163 cells, and white arrows represent a cell with no SERS signal but shows strong CD163 expression. (b) Quantification of DCFHDA fluorescence images of M2-like macrophages treated with Au@PGlyco NPs at 100 $ppm_{[Au]}$ for different time points. (c) Single-cell ROS levels in M2-like macrophages after treatment with 100 ppm Au@PGlyco NPs monitored by SERS-combined fluorescence imaging. Receiver operating characteristic (ROC) curves of the SERS intensity for the (d) M1/M2 ratio (n = 23) and (e) ROS level (n = 43) revealed Au@PGlyco NPs to be a good predictor of M2-to-M1 polarization in macrophages. The area under the curve (AUC) of the M1/M2 ratio was 0.865 ($p < 0.01$), whereas it was 0.735 for the ROS level ($p < 0.01$).

adequate SERS response signal intensity from the particle-treated T24 cells with low background noise. Figure 4c presents the SERS mapping images (at 1159 cm^{-1}) of T24 cells treated with different doses of the Au@PGlyco NPs, which depict the distribution of Au@PGlyco NPs-mediated SERS signals within the cells. The quantified SERS signal intensity allowed the SERS-targeted T24 cells to be sensed by using 1.25 $ppb_{[Au]}$ SERS probe/cell and subsequently experienced a dose-dependent increase (Figure 4d). Afterward, the bioimage of the Au@PGlyco NPs-mediated SERS intensity (at 1159 cm^{-1}) was recorded after treating mammalian cells, including Vero cells, HUVECs, and M2 macrophages, with Au@PGlyco NPs for 8 h (Figure 4e). The highest SERS intensity was detected in the T24 and M2-like macrophages (Figure 4d), which had higher SERS intensities than the Vero cells and HUVECs with the same treatment. This observation could be explained by the high expression of galactose-related receptors, such as galactose-type C-type lectin (MGL), on the M2-like macrophages;[36,64] these receptors could facilitate the internalization of Au@PGlyco NPs by receptor targeting. The parallel result by atomic absorption spectroscopy shows that the cell uptake of Au@PGlyco into the M2-like macrophages is 7.58×10^{-7} ppm/cell, which is 2.5−5.7-fold higher than the same incubation time with the galactose shell-free Au NPs at $1.33-3.02 \times 10^{-7}$ ppm/cell ppm (Figure S19).

Additionally, we observed the inhomogeneous SERS signals of the Au@PGlyco NPs across the whole cell body, as shown in Figure 4c,e; this observation suggested the different subcellular distributions of the NPs in different cell types. For example, the Au@PGlyco NPs that primarily accumulated in the nuclei of the HUVECs were visualized by the combination of SERS-labeling and Hoechst 33258-staining analysis in a high-magnification image (Figure 4f). It can also be seen that the SERS-based signal was adjacent to that of the cell membrane. In Vero cells and M2 macrophages, the SERS signal of the Au@PGlyco NPs appeared adjacent to that of the cell membrane in addition to cytosolic distribution rather than in the nucleus (Figure S20), suggesting that the Au@PGlyco NPs are present in different subcellular locations in different cell types.

Galactose is known as a proinflammatory factor for immune modulation.[65] We next performed a macrophage polarization test to investigate the bioactivity of galactose on the surface of Au@PGlyco NPs. Assisted by fluorescence staining with CD80 (M1-like macrophage marker, red fluorescence) and CD163 (M2-like macrophage marker, green fluorescence), M2-like macrophages treated with Au@PGlyco NPs presented higher

https://doi.org/10.1021/acsami.1c13647
ACS Appl. Mater. Interfaces 2021, 13, 52295−52307

red fluorescence and reduced green fluorescence with aging time compared with parent cells (Figures S21 and S22). This result showed that the Au@PGlyco NPs exhibited immunomodulatory activity for inducing inflammatory activation resulting from the M1-like polarization of macrophages. In parallel experiments of M2 macrophages cultured with Au@tannic acid (TNA), Au@TNA@PEG, Au@ONP-Glc, Au@PANI, and Au@ONP NPs, named based on the reacted precursors (Figure S23), the macrophages show no significant fluorescence changes in the ratio of CD80/CD163 markers compared with the particle-free treatment group (Figure S24). Interestingly, we also observed enhanced CD80 marker expression in M0-like macrophages after induction by Au@PGlyco NPs (8 h) to elicit inflammasome activation in macrophages (Figure S25).

Based on the sensitive SERS results of the Au@PGlyco NPs in cells, a tomographic mapping of the cells with high and low particle accumulations might be helpful in identifying downstream effects when single-cell responses are compared. To show this concept, M2-like macrophages treated with Au@PGlyco NPs and stained with CD80/CD163 markers were subjected to SERS image analysis (Figure 5a). Through the high spatial resolution of the SERS imaging, the individual M2 macrophages could be distinctly discriminated by the accumulation of Au@PGlyco NPs. The strong SERS signal in the cell images due to the higher loading of the Au@PGlyco NPs (labeled as red arrows) corresponds to the high red fluorescence of the M1 marker and low green fluorescence of the M2 marker. This imaging correlation is the high particle accumulation-induced M1 transition from M2. In contrast, the lower SERS intensity signal corresponds to the low red fluorescence and high green fluorescence of the macrophages in the cell images, indicating that the lower particle accumulation of Au@PGlyco NPs (labeled as green arrows) was insufficient for triggering the M2-to-M1 transition. A white arrow is used to label cells with a very low SERS signal, which were detected due to the high green fluorescence, which suggested the presence of few Au@PGlyco NPs within the cell, resulting in the presence of the M2-like macrophage phenotype and a lack of M1 stimulation effects.

To investigate the possible mechanism of the M2-to-M1 transition after Au@PGlyco NPs treatment, we used DCFHDA staining to investigate the generation of ROS (Figure 5b and Figure S26). Interestingly, the ROS expression level in M2 macrophages after Au@PGlyco NPs treatment exhibited a time-dependent increase. The particle-free treatment group (8 h) lacked significant green emission. However, the appearance of large error bars in Figure 5b might be due to the different uptake in each macrophage caused by the heterogeneity in the cell population.[66,67] It has been demonstrated that the cells that received the same stimulation can behave differently due to the different epigenetic regulation and growth period (unsynchronized cell cycle status) in single cells even from the same cell line.[31,67−69] This argument of cell heterogeneity was further examined through single-cell imaging analysis. Figure 5c shows the co-localization (8 h) of single-cell ROS levels in M2-like macrophages with real particle concentration administration using SERS-combined fluorescence imaging. These individual macrophage imaging examinations showed large generation of ROS from the high internalization of Au@PGlyco NPs.

Finally, the bio-analytical reliability of the Au@PGlyco NPs-SERS platform was studied. The approximate AUC (area under the curve) derived from the receiver operating characteristic (ROC) curve was subjected to assessment. The ROC curves were used to assess the discriminating capacity of SERS signals and the M1 macrophage polarization (by the M1/M2 ratio), and the AUC value was considered the prediction capacity for the macrophage polarization from unstimulated controls. As shown in Figure 5d, the AUC of the M1/M2 ratio is 0.865 ($p < 0.01$), suggesting that our method possessed a strong effect on the M1 macrophage polarization.[70] The specificity (true negative rate) and sensitivity (true positive rate) are 0.778 and 0.786, respectively, while the false positive rate is only 0.222, indicating that our method provided an acceptable model for macrophage polarization induction and prediction. Figure 5e shows 0.846 sensitivity and 0.529 specificity with 0.735 AUC according to the Au@PGlyco NPs-induced ROS levels. It is undeniable that transferring the absorbance of Au@PGlyco NPs to the NIR region can prevent the green fluorescence quenching during signal analysis, which would be beneficial to the further improvement of the ROC curves of future prediction models. In contrast to previous reports (Table S1) with our work, this SERS imaging application with single-cell immunity platform is the first report on the heterogeneity of macrophages in relation with the internalization of Au@PGlyco NPs for the transition status of particle-modulated macrophages.

Again, the bacteria determination assessment was analyzed in Figure S27. The AUC of the ROC curve is 0.901 ($p < 0.001$) with 0.813 specificity and 0.833 sensitivity. Through the specific bio-cleavage via the β-gal enzyme (Figure 3g), the turn-off signal change of the Au@PGlyco NPs has the expected good discriminating capacity in live bacteria detection.

3. CONCLUSIONS

We successfully developed an in situ hybridization of glycopolymer/Au NPs with ortho-nitrophenyl functional glucoside and galactoside that could be applied to other ortho-nitrophenyl compounds for evolving intrinsic PANI-based SERS. Relying on the galactose moiety, the Au@PGlyco NPs acted as a novel bio-SERS probe to sense bacteria in concentrations of at least 10^2 CFU/mL and exhibited exceptional imaging ability toward living cells by targeting galactose-binding receptors and particle internalization. The sensing platform of Au@PGlyco NPs was promising for deeper exploration of the intracellular mechanisms with exogenous biomolecules with a positive correlation of uptake concentrations with downstream biological reactions based on insights into single-cell detection using galactose-responsive SERS monitoring. Au@PGlyco NPs may promote the production of ROS via interaction with a galactose-binding receptor and thus trigger the macrophage reprogramming transition to the immunogenic type (M1), providing the potential applications of immunomodulation.

4. MATERIALS AND METHODS

4.1. Chemicals and Materials. Hydrogen tetrachloroaurate(III) trihydrate ($HAuCl_4 \cdot 3H_2O$, 99%) and 3-(4,5-dimethylthiazol-2-yl)-2,5-diphenyltetrazolium bromide (MTT assay reagent) were from Alfa Aesar. Ethanol (95%) was from J.T. Baker. 2-Nitrophenyl-β-galactoside (ONPG, >99%), 4-nitrophenyl-β-galactoside (PNPG, 99.9%), and 2-nitrophenyl-β-glucopyranoside (ONP-Glc) were from Biosynth Carbosynth. Hydrogen peroxide solution (H_2O_2, 34.5−36.5%), β-galactosidase (β-gal, from *E. coli*), polyaniline emeraldine base (PANI, $M_w \approx 5000$), and malachite green (MG) oxalate salt

https://doi.org/10.1021/acsami.1c13647
ACS Appl. Mater. Interfaces 2021, 13, 52295−52307

(>90%) were from Sigma-Aldrich. Sodium terahydridoborate ($NaBH_4$) was from Riedel-de Haen, and 2-nitrophenol (ONP, 99%) and 4-nitrophenol (PNP, 99%) were from Acros Organics. D-(+)-Galactose anhydrous (>98%) was from TCI, Luria-Bertani (LB) broth was from AthenaES, and phosphate-buffered saline (PBS, pH 7.0) was from Thermo. Aqueous solutions were prepared using deionized H_2O (DI water). McCoy's 5a, Dulbecco's modification of Eagle's medium (DMEM), and Roswell Park Memorial Institute (RPMI) medium were from Corning.

4.2. Preparation of the Au@PGlyco NPs. The synthesis of Au@PGlyco NPs was prepared by heating 10 mL of $HAuCl_4$ solution (1 mM) in an oil bath at 80 °C with magnetic stirring for 10 min followed by addition of 1 mL of ONPG solution (100, 80, 60, 30, 15, 5, and 1 mM). After another 10 min of heating, 0.2 mL of $NaBH_4$ (20 mM) as the reducing agent was subsequently added into the above stock solution for 1 min. The stock solution was cooled down to room temperature under 60 min of stirring. To purify the samples, the stock solution was centrifuged at 6000 rpm for 10 min, thus the supernatant was removed, and the resulting pellet was resuspended in DI water. This purification was repeated three times. The purified samples were stored in DI water at 4 °C for further use. To evaluate the formation of Au@PGlyco NPs, ONPG was replaced with 80 mM PNPG, PANI, ONP, PNP, galactose, ONP-Glc, and 19.3 mM PANI with the same synthesis conditions.

4.3. Characterization. The nanoparticle images were studied by transmission electron microscopy (TEM, Hitachi H-7500) at 80 keV and scanning electron microscopy (SEM, JSM-6700F) at 10 keV. Energy-dispersive spectrometry (EDS) measurements for detecting Au and N elements were performed by high-resolution transmission electron microscopy (HR-TEM, JEOL-2100F). The absorption spectra were recorded using an ultraviolet−visible spectrophotometer (UV−vis, JASCO V-730). The Au concentrations of the Au-based materials were quantified by atomic absorption spectroscopy (AAS, SensAA GBC). The crystalline structure of nanoparticles was characterized by X-ray diffraction on a multipurpose X-ray thin-film diffractometer (XRD, Rigaku). The FT-IR spectra of dried samples were obtained using Fourier-Transform Infrared spectroscopy (FT-IR, JASCO-4700). The chemical state of nitrogen was identified by X-ray photoelectron spectroscopy (XPS, Thermo Fisher Scientific ESCALAB Xi^+). The hydrodynamic diameter and polydispersity index (PDI) of Au@PGlyco NPs were measured by a dynamic light scattering spectrometer (DLS, Malvern, U.K., Zetasizer Nano ZS90). The content of the organic composite layer at the surface of Au@PGlyco NPs was weighted by thermogravimetric analysis (TGA) using a TA-Q50 thermogravimetric analyzer at a ramp rate of 20 °C min^{-1} in air.

4.4. SERS Measurement of Solution Samples. The SERS spectra were measured using a portable 671 nm Raman system (LiveStrong Optoelectronics, LS-PT 671) assembled with a power-adjustable 671 nm laser (100 mM, 0.1 nm full width at half-maximum) and a low noise spectrometer module (<13 cm^{-1} resolution). All samples were prepared in DI water with the desired concentration, and a 10 μL aliquot of respective solution was dropped onto a silicon substrate. SERS spectra were subsequently acquired on a portable-Raman spectrometer using a 671 nm excitation laser with 100 mW power. The spectra were employed with an acquisition time of 1 s with three accumulations.

To evaluate the Raman reproducibility of Au@PGlyco NPs, 20 synthetic batches of Au@PGlyco NPs with 15 $ppm_{[Au]}$ were measured at 671 nm excitation. The SERS intensity at 1159 cm^{-1} was recorded and plotted versus the number of sample batches. The relative standard deviation (RSD) was further calculated.

The colloidal stabilities of 30 $ppm_{[Au]}$ Au@PGlyco NPs in H_2O, PBS, cell culture media (McCoy's 5a, RPMI, and DMEM), and 0.1 mM H_2O_2 were evaluated using SERS measurement. The Au@PGlyco NPs was incubated in these solutions for 0, 2, 8, and 24 h at 37 °C for subsequent SERS measurement at 671 nm excitation.

4.5. Calculations of the Enhancement Factor (EF) and Analytical Enhancement Factor (AEF). The values of the EF and AEF were obtained experimentally using the following equation:

$$\mathrm{EF} = \frac{I_{\mathrm{SERS}} \times C_{\mathrm{normal}}}{I_{\mathrm{normal}} \times C_{\mathrm{SERS}}} \quad (1)$$

To determine the EF of Au@PGlyco NPs, the intrinsic PGlyco molecules were examined in the calculation, where I_{SERS} is the SERS intensity of Au@PGlyco NPs at 1159 cm^{-1} and I_{normal} is the Raman intensity of pure PANI molecules at 1159 cm^{-1} (Figure S12a). C_{SERS} of the PGlyco concentration was estimated at 0.51 ppm by using 9 $ppm_{[Au]}$ Au@PGlyco NPs according to the TGA measurement (Figure S3a), and C_{normal} is the concentration of pure PANI molecules at 1860 ppm. To simplify the computational complexity to ignore the polymer molecular weight range and molecular structure of the PGlyco polymer structure, we quantified the glycopolymer weight by TGA as comparison units and took the pure PANI at 1860 ppm as a computational comparison.

The external malachite green (MG) was further examined for calculating the AEF value of Au@PGlyco NPs, where I_{SERS} is the SERS intensity of MG at 797 cm^{-1} with 30 $ppm_{[Au]}$ Au@PGlyco NPs, I_{normal} is the Raman intensity of pure MG molecules at 797 cm^{-1}, C_{SERS} is the concentration of MG at 1 nM, and C_{normal} is the concentration of MG at 10 μM (Figure S12b,c). This AEF measurement provided a simple method in the liquid phase for the reproducible and reliable comparison of the Raman enhanced activity between the molecules in the solution and the colloidal subtract sample.[71]

4.6. SERS Detection of β-Galactosidase (β-Gal) Using Au@PGlyco NPs. The β-gal with a series of concentrations (nM) was accessed by measuring the SERS intensity change at 1159 cm^{-1} of Au@PGlyco NPs reacted with β-gal. To investigate the enzymatic response of Au@PGlyco NPs over time, 100 μL of β-gal solution (20 μM) was added into 100 μL of Au@PGlyco solution with 30 $ppm_{[Au]}$. The SERS spectra of the mixture were recorded at 0, 1, 10, 30, and 60 min of incubation using the 671 nm portable-Raman system. To investigate the dynamic relationship between the β-gal concentration and SERS intensity of Au@PGlyco NPs, 100 μL of β-gal solution (1, 2, 3, 4, and 5 nM) was added into 100 μL of Au@PGlyco solution with 30 $ppm_{[Au]}$. After 60 min of incubation, 10 μL aliquot of each solution was measured using the 671 nm portable-Raman system. The dynamic relationship of the β-gal concentration versus the SERS intensity of Au@PGlyco NPs was plotted.

4.7. Bacterial Cultivation and SERS-Based Measurement. *E. coli* was cultured in LB broth medium overnight at 37 °C. Gram-negative bacterium *E. coli* O157:H7 was centrifuged at 8500 rpm for 5 min and re-suspended in PBS buffer more than three times for subsequent quantification with optical density at 600 nm (OD_{600}) using a microplate reader (BioTek/SYNERGY-H1). For determining the number of bacterial cells, 100 μL of bacterial suspension (10^8, 10^4, 10^3, 10^2, and 10^1 CFU/mL) was added into 100 μL of Au@PGlyco solution with 12 $ppm_{[Au]}$ for measuring the SERS intensity of Au@PGlyco NPs. The SERS spectrum of a 10 μL aliquot mixture was measured using a 671 nm portable-Raman spectrometer after 1 and 6 h of incubation at room temperature.

4.8. Bacterial Viability. The bacterial viability of *E. coli* mixed with Au@PGlyco NPs was calculated by culturing bacteria on an LB agar plate. Briefly, 100 μL of bacterial suspension (10^4 CFU/mL) was added into 100 μL of Au@PGlyco NPs (12, 18, 24, and 30 $ppm_{[Au]}$) for incubation at 37 °C overnight. After incubation, the mixture was centrifuged at 8500 rpm for 5 min and resuspended in PBS. Then, 100 μL aliquot of the mixture was plated on an LB agar plate for bacterial cultivation. The number of bacterial colonies was counted after 24 h of cultivation, and the bacterial viability was recorded. To further confirm the bacterial morphology after incubation with Au@PGlyco NPs, 100 μL of bacterial suspension (10^6 CFU/mL) was added into 100 μL of Au@PGlyco NPs (30 $ppm_{[Au]}$) incubated at 37 °C overnight for TEM images.

4.9. Cell Culture. T24 (human bladder cancer cell), Hela (human cervical cancer cell), Vero (monkey epithelium cell), HUVEC (human endothelium cell), and THP-1 (human macrophage) cells (American Type Culture Collection, Manassas, VA) were cultured with McCoy's 5a medium (T24), Dulbecco's Modified Eagle's

https://doi.org/10.1021/acsami.1c13647
ACS Appl. Mater. Interfaces 2021, 13, 52295−52307

Medium (DMEM) (Hela, Vero, and HUVEC), and RPMI-1640 medium (THP-1) supplemented with 10% fetal bovine serum (FBS) and a 1% antibiotic-antimycotic agent. All cell lines were maintained in a 37 °C incubator with a humidified environment of 5% CO_2 atmosphere.

4.10. Macrophage Differentiation and Polarization. THP-1 monocytes were cultured in RPMI-1640 medium with 100 nM phorbol 12-myristate 13-acetate (PMA) for 24 h to induce M0 differentiation and then subsequently stimulated by 20 nM IL-4 for 48 h to induce M2 polarization. The resulting M0 and M2 macrophages were subjected for further SERS experiments.

4.11. SERS Detection and Mapping of Living Cells. Cells (1×10^5) were seeded on a 3.5 cm glass bottom dish (Alpha Plus) and treated with Au@PGlyco NPs (100 $ppm_{[Au]}$) for 8 h, and then cells were washed with phosphate buffered saline (PBS) and subjected for SERS detection by a microscope (Olympus IX73) equipped with spectrometers (MRS-iHR 320). The Raman signals were acquired using 671 nm laser with 3 mW for 1 s acquisition. For SERS signal mapping of cells, the same condition was applied with 40×40 pixels for 200×200 μm^2 (low resolution) and 40×40 μm^2 (high resolution). The signals at 1159 cm^{-1} were subjected to heat mapping of living cells.

4.12. Fluorescence Microscopy for Macrophage Polarization Observation. The macrophages treated with Au@PGlyco NPs were washed and fixed by 4% paraformaldehyde at 4 °C for 10 min and then incubated with 1% bovine serum albumin (BSA) for 1 h at room temperature to block non-specific antibody binding. After BSA blocking, cells were washed three times by PBS and incubated with anti-CD80 (rabbit, 1:200 dilution, Abcam) and anti-CD163 (mouse, 1:200 dilution, Invitrogen) antibody at 4 °C overnight. Finally, the cells bound with a primary antibody were subsequently incubated with a secondary antibody conjugated with Alexa Fluor 594 (red fluorescence for CD-80 recognition) or Alexa Fluor 488 (green fluorescence for CD163 recognition) for 1 h at room temperature. The stained macrophages were measured by a fluorescence microscope (Olympus IX73).

4.13. Cell Viability. Human umbilical vein endothelial cells (HUVEC), HeLa cells, Vero cells, and human urinary bladder cells (T24) were used to study the cytotoxicity of Au@PGlyco NPs on mammalian cells. The cells (8×10^3) were seeded in a 96-well plate overnight. The cells were incubated with 0−100 $ppm_{[Au]}$ of Au@PGlyco NPs. After incubating for 24 h, the Au@PGlyco NPs-containing medium was replaced with a fresh medium. The MTT reagent (1.2 mM) was added into each well, and cells were further incubated for 1 h After removing the medium, DMSO was added into each well to dissolve formazan crystals. Finally, the absorbance was measured at 565 nm with a microplate reader (Synergy H1, BioTek) and the cell viability was calculated.

4.14. Fluorescence Microscopy for ROS Generation. T24, HUVEC, and Vero cells were treated with Au@PGlyco NPs (100 $ppm_{[Au]}$) for 8 h. Additionally, M2-polarized THP-1 were treated with the same concentration of Au@PGlyco NPs for 45 min, 1 h, 2 h, 4 h, and 8 h. After treatment, cells were then stained by 10 μM DCFHDA dye for 30 min and imaged by a fluorescence microscope.

4.15. Cell Uptake Experiment. The macrophages were treated with 100 ppm Au@tannic acid (TNA), Au@TNA@PEG, Au@PGlyco, Au@2NP, Au@TNA, or Au@TNA@PEG NPs for 8 h and subsequently dissolved in 12 M HCl. The dissolved solutions were subjected to the uptake NPs measurement by atomic absorption spectroscopy (AAS) for Au concentration determination.

The Au@TNA and Au@TNA@PEG NPs were prepared according to the previous report,[72] which was kindly provided by Prof Mei-Yi Liao at National Pingtung University (Taiwan).

4.16. Statistical Methods. Statistical analyses were performed using Prism (version 7; GraphPad, San Diego, CA, USA). The ROC curves were used to assess the discriminating capacity of the SERS signals from Au@PGlyco NPs in bacteria detection, the ROS level, and macrophage polarization status (M1/M2). The AUC value was considered the prediction capacity for the bacteria treatment group from bacteria-free control and the macrophage polarization ratio (M1/M2) from untreated M2 macrophages. An AUC greater than 0.9 indicated excellent prediction efficacy, and an AUC between 0.7 and 0.9 indicated good efficacy. An AUC between 0.5 and 0.7 indicated poor diagnostic efficacy, an AUC under 0.5 indicated the lack of a diagnostic value of the prediction model, and p value <0.05 was considered to represent statistical significance.[73,74]

4.17. Computational Details. All density functional theory (DFT) calculations were carried out by means of the Gaussian 16 package, adopting the B3LYP hybrid exchange and correlation functional and LANL2DZ basis set. The optimized geometries correspond to true energy minima by considering that all vibrational frequencies were real and positive.

■ ASSOCIATED CONTENT

Supporting Information

The Supporting Information is available free of charge at https://pubs.acs.org/doi/10.1021/acsami.1c13647.

XRD spectra, SERS spectra, calculated Raman spectra of DFT-optimized structures, TEM images, and UV−visible spectra of Au@PGlyco and Au-based NPs; setup of in situ SERS measurement for the formation of Au@PGlyco NPs; time-dependent 671 nm Raman measurements of bacteria, bacterial viability, and TEM images for Au@PGlyco NPs-treated *E. coli*; dose-dependent UV−visible measurement of ONPG; and in vitro co-localized SERS images, bright field images, and fluorescence images of Au@PGlyco and Au-based NPs-treated cells (PDF)

Low and inconsistent SERS response from the close attachment between the Au core and ONPG molecules (MP4)

Reaction observation for the immediate generation of the dark-red Au colloid and SERS response of Au@PGlyco NPs after the addition of $NaBH_4$ (MP4)

■ AUTHOR INFORMATION

Corresponding Author

Chih-Chia Huang − *Department of Photonics and Center of Applied Nanomedicine, National Cheng Kung University, Tainan 70101, Taiwan;* orcid.org/0000-0002-9486-8665; Email: c2huang@email.ncku.edu.tw, huang.chihchia@gmail.com

Authors

Zi-Chun Chia − *Department of Photonics, National Cheng Kung University, Tainan 70101, Taiwan*

Li-Xing Yang − *Department of Photonics, National Cheng Kung University, Tainan 70101, Taiwan*

Ting-Yu Cheng − *Department of Photonics, National Cheng Kung University, Tainan 70101, Taiwan*

Ya-Jyun Chen − *Department of Photonics, National Cheng Kung University, Tainan 70101, Taiwan*

Horng-Long Cheng − *Department of Photonics, National Cheng Kung University, Tainan 70101, Taiwan*

Fei-Ting Hsu − *Department of Biological Science and Technology, China Medical University, Taichung 40402, Taiwan*

Ying-Jan Wang − *Department of Environmental and Occupational Health, National Cheng Kung University, Tainan 70101, Taiwan*

Yu-Ying Chen − *Department of Environmental and Occupational Health, National Cheng Kung University, Tainan 70101, Taiwan*

Tzu-Chi Huang − *Department of Photonics, National Cheng Kung University, Tainan 70101, Taiwan*
Yi-Syun Fang − *Department of Photonics, National Cheng Kung University, Tainan 70101, Taiwan*

Complete contact information is available at: https://pubs.acs.org/10.1021/acsami.1c13647

Author Contributions

⊥Z.-C.C. and L.-X.Y. contributed equally to this work. Z.-C.C. carried out the bacterial experiments, material synthesis, and sample optical characterizations and wrote the draft of the manuscript. L.-X.Y. carried out the cell experiments, fluorescence cellular imaging analysis, and statistical analysis and wrote the draft of the manuscript. T.-Y.C. carried out the surface enhanced Raman scattering (SERS) and cellular SERS experiments and performed the synthesis and characterizations. Y.-J.C. carried out the bacterial experiments and wrote the draft of the manuscript. H.-L.C. carried out the density functional theory calculations. F.-T.H. carried out the immunogenic M1/M2 macrophage transition experiments and reviewed and edited this paper. Y.-J.W. carried out the cell experiments. Y.-Y.C. carried out the cell experiments. T.-C.H. carried out the material synthesis and sample characterizations. Y.-S.F. carried out the in situ SERS examination. C.-C.H. wrote the draft of the manuscript, reviewed and edited this paper, and supervised and designed this research.

Notes

The authors declare no competing financial interest.

■ ACKNOWLEDGMENTS

This work was supported in part by grants from the Ministry of Science and Technology, Taiwan (MOST 108-2113-M-006-012-MY3, MOST 109-2327-B-009-001, MOST 108-2314-B-039-007-MY3, and MOST 109-2221-E-006-149). This work was financially supported by the Center of Applied Nanomedicine, National Cheng Kung University from the Featured Areas Research Center Program within the framework of the Higher Education Sprout Project by the Ministry of Education (MOE) in Taiwan. We thank Prof. Chia-Chih Chang, Prof. Ho-Hsiu Chou, and Prof. Ying-Nien Chou for valuable support with polyaniline. We are grateful to the National Center for High-Performance Computing of Taiwan for computer time and facilities.

■ REFERENCES

(1) Werz, D. B.; Seeberger, P. H. Carbohydrates as the Next Frontier in Pharmaceutical Research. *Chem. − Eur. J.* **2005**, *11*, 3194−3206.
(2) Spain, S. G.; Gibson, M. I.; Cameron, N. R. Recent Advances in the Synthesis of Well-Defined Glycopolymers. *J.Polym. Sci., A: Polym. Chem.* **2007**, *45*, 2059−2072.
(3) Becer, C. R. The Glycopolymer Code: Synthesis of Glycopolymers and Multivalent Carbohydrate-Lectin Interactions. *Macromol. Rapid Commun.* **2012**, *33*, 742−752.
(4) Qi, W.; Zhang, Y.; Wang, J.; Tao, G.; Wu, L.; Kochovski, Z.; Gao, H.; Chen, G.; Jiang, M. Deprotection-Induced Morphology Transition and Immunoactivation of Glycovesicles: A Strategy of Smart Delivery Polymersomes. *J. Am. Chem. Soc.* **2018**, *140*, 8851−8857.
(5) Yuan, S. S.; Li, M. L.; Chen, J. S.; Zhou, L.; Zhou, W. Application of Mono- and Disaccharides in Drug Targeting and Efficacy. *ChemMedChem* **2018**, *13*, 764−778.
(6) Jain, A.; Jain, A.; Parajuli, P.; Mishra, V.; Ghoshal, G.; Singh, B.; Shivhare, U. S.; Katare, O. P.; Kesharwani, P. Recent Advances in Galactose-Engineered Nanocarriers for the Site-Specific Delivery of siRNA and Anticancer Drugs. *Drug Discovery Today* **2018**, *23*, 960−973.
(7) Kawakami, S.; Hashida, M. Glycosylation-Mediated Targeting of Carriers. *J. Controlled Release* **2014**, *190*, 542−555.
(8) Mukherjee, M. B.; Mullick, R.; Reddy, B. U.; Das, S.; Raichur, A. M. Galactose Functionalized Mesoporous Silica Nanoparticles As Delivery Vehicle in the Treatment of Hepatitis C Infection. *ACS Appl. Bio Mater.* **2020**, *3*, 7598−7610.
(9) Zhao, Y.; Guo, Q.; Dai, X.; Wei, X.; Yu, Y.; Chen, X.; Li, C.; Cao, Z.; Zhang, X. A Biomimetic Non-Antibiotic Approach to Eradicate Drug-Resistant Infections. *Adv. Mater.* **2019**, *31*, No. e1806024.
(10) Kiessling, L. L.; Grim, J. C. Glycopolymer Probes of Signal Transduction. *Chem. Soc. Rev.* **2013**, *42*, 4476−4491.
(11) Poonthiyil, V.; Golovko, V. B.; Fairbanks, A. J. Size-optimized Galactose-Capped Gold Nanoparticles for the Colorimetric Detection of Heat-Labile Enterotoxin at Nanomolar Concentrations. *Org. Biomol. Chem.* **2015**, *13*, 5215−5223.
(12) Edwards, K. A. Periplasmic-Binding Protein-Based Biosensors and Bioanalytical Assay Platforms: Advances, Considerations, and Strategies for Optimal Utility. *Talanta Open* **2021**, *3*, 100038.
(13) Bartneck, M.; Heffels, K. H.; Pan, Y.; Bovi, M.; Zwadlo-Klarwasser, G.; Groll, J. Inducing Healing-Like Human Primary Macrophage Phenotypes by 3D Hydrogel Coated Nanofibres. *Biomaterials* **2012**, *33*, 4136−4146.
(14) Wu, L.; Zhang, Y.; Li, Z.; Yang, G.; Kochovski, Z.; Chen, G.; Jiang, M. ″Sweet″ Architecture-Dependent Uptake of Glycocalyx-Mimicking Nanoparticles Based on Biodegradable Aliphatic Polyesters by Macrophages. *J. Am. Chem. Soc.* **2017**, *139*, 14684−14692.
(15) Zhang, Y.; Wu, L.; Li, Z.; Zhang, W.; Luo, F.; Chu, Y.; Chen, G. Glycocalyx-Mimicking Nanoparticles Improve Anti-PD-L1 Cancer Immunotherapy through Reversion of Tumor-Associated Macrophages. *Biomacromolecules* **2018**, *19*, 2098−2108.
(16) Ding, Y.; Liang, J. J.; Geng, D. D.; Wu, D.; Dong, L.; Shen, W. B.; Xia, X. H.; Zhang, C. Development of a Liver-Targeting Gold-PEG-Galactose Nanoparticle Platform and a Structure-Function Study. *Part. Part. Syst. Charact.* **2014**, *31*, 347−356.
(17) Hao, N.; Neranon, K.; Ramström, O.; Yan, M. Glyconanomaterials for Biosensing Applications. *Biosens. Bioelectron.* **2016**, *76*, 113−130.
(18) Tunki, L.; Kulhari, H.; Vadithe, L. N.; Kuncha, M.; Bhargava, S.; Pooja, D.; Sistla, R. Modulating the Site-Specific Oral Delivery of Sorafenib using Sugar-Grafted Nanoparticles for Hepatocellular Carcinoma Treatment. *Eur. J. Pharm. Sci.* **2019**, *137*, 104978.
(19) Huang, K.-W.; Lai, Y.-T.; Chern, G.-J.; Huang, S.-F.; Tsai, C.-L.; Sung, Y.-C.; Chiang, C.-C.; Hwang, P.-B.; Ho, T.-L.; Huang, R.-L.; Shiue, T.-Y.; Chen, Y.; Wang, S.-K. Galactose Derivative-Modified Nanoparticles for Efficient siRNA Delivery to Hepatocellular Carcinoma. *Biomacromolecules* **2018**, *19*, 2330−2339.
(20) Mamidyala, S. K.; Dutta, S.; Chrunyk, B. A.; Préville, C.; Wang, H.; Withka, J. M.; McColl, A.; Subashi, T. A.; Hawrylik, S. J.; Griffor, M. C.; Kim, S.; Pfefferkorn, J. A.; Price, D. A.; Menhaji-Klotz, E.; Mascitti, V.; Finn, M. G. Glycomimetic Ligands for the Human Asialoglycoprotein Receptor. *J. Am. Chem. Soc.* **2012**, *134*, 1978−1981.
(21) de la Fuente, J. M.; Barrientos, A. G.; Rojas, T. C.; Rojo, J.; Canada, J.; Fernandez, A.; Penades, S. Gold Glyconanoparticles as Water-Soluble Polyvalent Models to Study Carbohydrate Interactions. *Angew. Chem., Int. Ed.* **2001**, *40*, 2258−2261.
(22) Zhu, C.-D.; Zheng, Q.; Wang, L.-X.; Xu, H.-F.; Tong, J.-L.; Zhang, Q.-A.; Wan, Y.; Wu, J.-Q. Synthesis of Novel Galactose Functionalized Gold Nanoparticles and its Radiosensitizing Mechanism. *J. Nanobiotechnol.* **2015**, *13*, 1−11.
(23) Jung, J.; Park, S.; Hong, S.; Ha, M. W.; Park, H. G.; Park, Y.; Lee, H. J.; Park, Y. Synthesis of Gold Nanoparticles with Glycosides: Synthetic Trends Based on the Structures of Glycones and Aglycones. *Carbohydr. Res.* **2014**, *386*, 57−61.
(24) Martin-Trasanco, R.; Cao, R.; Esparza-Ponce, H. E.; Montero-Cabrera, M. E.; Arratia-Pérez, R. Reduction of Au(III) by a Beta-

Cyclodextrin Polymer in Acid Medium. A Stated Unattainable Reaction. *Carbohydr. Polym.* **2017**, *175*, 530−537.
(25) Mei, R.; Wang, Y.; Liu, W.; Chen, L. Lipid Bilayer-Enabled Synthesis of Waxberry-Like Core-Fluidic Satellite Nanoparticles: Toward Ultrasensitive Surface-Enhanced Raman Scattering Tags for Bioimaging. *ACS Appl. Mater. Interfaces* **2018**, *10*, 23605−23616.
(26) Chen, G.; Wang, Y.; Yang, M.; Xu, J.; Goh, S. J.; Pan, M.; Chen, H. Measuring Ensemble-Averaged Surface-Enhanced Raman Scattering in the Hotspots of Colloidal Nanoparticle Dimers and Trimers. *J. Am. Chem. Soc.* **2010**, *132*, 3644−3645.
(27) Wang, J.; Wu, X.; Wang, C.; Shao, N.; Dong, P.; Xiao, R.; Wang, S. Magnetically Assisted Surface-Enhanced Raman Spectroscopy for the Detection of Staphylococcus aureus Based on Aptamer Recognition. *ACS Appl. Mater. Interfaces* **2015**, *7*, 20919−20929.
(28) Wang, Y.; Yan, B.; Chen, L. X. SERS Tags: Novel Optical Nanoprobes for Bioanalysis. *Chem. Rev.* **2013**, *113*, 1391−1428.
(29) Lee, C. W.; Ko, H.; Chang, S. H. G.; Huang, C. C. Invisible-Ink-Assisted Pattern and Written Surface-Enhanced Raman Scattering Substrates for Versatile Chem/Biosensing Platforms. *Green Chem.* **2018**, *20*, 5318−5326.
(30) Lee, C.-W.; Chia, Z. C.; Hsieh, Y.-T.; Tsai, H.-C.; Tai, Y.; Yu, T.-T.; Huang, C.-C. A Facile Wet-Chemistry Approach to Engineer an Au-Based SERS Substrate and Enhance Sensitivity Down to ppb-level Detection. *Nanoscale* **2021**, *13*, 3991−3999.
(31) Aioub, M.; El-Sayed, M. A. A Real-Time Surface Enhanced Raman Spectroscopy Study of Plasmonic Photothermal Cell Death Using Targeted Gold Nanoparticles. *J. Am. Chem. Soc.* **2016**, *138*, 1258−1264.
(32) Haldavnekar, R.; Venkatakrishnan, K.; Tan, D. B. Boosting the Sub-Cellular Biomolecular Cancer Signals by Self-Functionalized Tag-Free Nano Sensor. *Biosens. Bioelectron.* **2021**, *190*, 113407.
(33) Wallace, G. Q.; Masson, J. F. From Single Cells to Complex Tissues in Applications of Surface-Enhanced Raman Scattering. *Analyst* **2020**, *145*, 7162−7185.
(34) Mei, R.; Wang, Y.; Yu, Q.; Yin, Y.; Zhao, R.; Chen, L. Gold Nanorod Array-Bridged Internal-Standard SERS Tags: From Ultrasensitivity to Multifunctionality. *ACS Appl. Mater. Interfaces* **2020**, *12*, 2059−2066.
(35) Lin, D.; Qin, T.; Wang, Y.; Sun, X.; Chen, L. Graphene Oxide Wrapped SERS Tags: Multifunctional Platforms toward Optical Labeling, Photothermal Ablation of Bacteria, and the Monitoring of Killing Effect. *ACS Appl. Mater. Interfaces* **2014**, *6*, 1320−1329.
(36) Roszer, T. Understanding the Mysterious M2 Macrophage through Activation Markers and Effector Mechanisms. *Mediators Inflammation* **2015**, *2015*, 816460.
(37) Sindram, J.; Krüsmann, M.; Otten, M.; Pauly, T.; Nagel-Steger, L.; Karg, M. Versatile Route toward Hydrophobically Polymer-Grafted Gold Nanoparticles from Aqueous Dispersions. *J. Phys. Chem. B* **2021**, *125*, 8225−8237.
(38) Liu, Y.; Shipton, M. K.; Ryan, J.; Kaufman, E. D.; Franzen, S.; Feldheim, D. L. Synthesis, Stability, and Cellular Internalization of Gold Nanoparticles Containing Mixed Peptide-Poly(ethylene glycol) Monolayers. *Anal. Chem.* **2007**, *79*, 2221−2229.
(39) Mondal, P.; Guo, C.; Yarger, J. L. Water Soluble Gold-Polyaniline Nanocomposite: A Substrate for Surface Enhanced Raman Scattering and Catalyst for Dye Degradation. *Arab. J. Chem.* **2020**, *13*, 4009−4018.
(40) Sreedhar, B.; Sairam, M.; Chattopadhyay, D. K.; Mitra, P. P.; Rao, D. V. M. Thermal and XPS Studies on Polyaniline Salts Prepared by Inverted Emulsion Polymerization. *J. Appl. Polym. Sci.* **2006**, *101*, 499−508.
(41) Meenakshi, R. Experimental (FT-IR and FT-Raman) and Spectroscopic Investigations, Electronic Properties and Conformational Analysis by PES Scan on 2-methoxy-5-nitrophenol and 2-methoxy-4-methylphenol. *RSC Adv.* **2016**, *6*, 21822−21831.
(42) Perez-Jimenez, A. I.; Lyu, D.; Lu, Z.; Liu, G.; Ren, B. Surface-Enhanced Raman Spectroscopy: Benefits, Trade-offs and Future Developments. *Chem. Sci.* **2020**, *11*, 4563−4577.
(43) Nobrega, M. M.; Souza, K. S.; Andrade, G. F. S.; Camargo, P. H. C.; Temperini, M. L. A. Emeraldine Salt Form of Polyaniline as a Probe Molecule for Surface Enhanced Raman Scattering Substrates Excited at 1064 nm. *J. Phys. Chem. C* **2013**, *117*, 18199−18205.
(44) Kurouski, D.; Large, N.; Chiang, N.; Greeneltch, N.; Carron, K. T.; Seideman, T.; Schatz, G. C.; Van Duyne, R. P. Unraveling Near-Field and Far-Field Relationships for 3D SERS Substrates - a Combined Experimental and Theoretical Analysis. *Analyst* **2016**, *141*, 1779−1788.
(45) Braun, G. B.; Lee, S. J.; Laurence, T.; Fera, N.; Fabris, L.; Bazan, G. C.; Moskovits, M.; Reich, N. O. Generalized Approach to SERS-Active Nanomaterials via Controlled Nanoparticle Linking, Polymer Encapsulation, and Small-Molecule Infusion. *J. Phys. Chem. C* **2009**, *113*, 13622−13629.
(46) Morávková, Z.; Dmitrieva, E. The First Products of Aniline Oxidation - SERS Spectroelectrochemistry. *ChemistrySelect* **2019**, *4*, 8847−8854.
(47) Trchová, M.; Morávková, Z.; Bláha, M.; Stejskal, J. Raman Spectroscopy of Polyaniline and Oligoaniline Thin Films. *Electrochim. Acta* **2014**, *122*, 28−38.
(48) Jiao, L.-S.; Wang, Z.; Niu, L.; Shen, J.; You, T.-Y.; Dong, S.-J.; Ivaska, A. In Situ Electrochemical SERS Studies on Electrodeposition of Aniline on 4-ATP/Au Surface. *J. Solid State Electrochem.*. **2006**, *10*, 886−893.
(49) Golczak, S.; Kanciurzewska, A.; Fahlman, M.; Langer, K.; Langer, J. J. Comparative XPS Surface Study of Polyaniline Thin Films. *Solid State Ionics* **2008**, *179*, 2234−2239.
(50) Kabir, S.; Artyushkova, K.; Serov, A.; Kiefer, B.; Atanassov, P. Binding Energy Shifts for Nitrogen-Containing Graphene-Based Electrocatalysts - Experiments and DFT Calculations. *Surf. Interface Anal.* **2016**, *48*, 293−300.
(51) Huang, W. S.; Sun, I. W.; Huang, C. C. Promotion of SERS and Catalytic Activities with Bimetallic and Ternary Concave Nanolayers. *J. Mater. Chem. A* **2018**, *6*, 13041−13049.
(52) Bicak, T. C.; Soylemez, S.; Buber, E.; Toppare, L.; Yagci, Y. Poly(o-aminophenol) Prepared by Cu(II) Catalyzed Air Oxidation and its Use as a Bio-Sensing Architecture. *Polym. Chem.* **2017**, *8*, 3881−3888.
(53) Davidson, R. A.; Guo, T. An Example of X-ray Nanochemistry: SERS Investigation of Polymerization Enhanced by Nanostructures under X-ray Irradiation. *J. Phys. Chem. Lett.* **2012**, *3*, 3271−3275.
(54) Nobrega, M. M.; Martins, V. L.; Torresi, R. M.; Temperini, M. L. A. One-Step Synthesis, Characterization, and Properties of Emeraldine Salt Nanofibers Containing Gold Nanoparticles. *J. Phys. Chem. C* **2014**, *118*, 4267−4274.
(55) Zhu, W.; Dong, Z.; Fu, T.; Liu, J.; Chen, Q.; Li, Y.; Zhu, R.; Xu, L.; Liu, Z. Modulation of Hypoxia in Solid Tumor Microenvironment with MnO_2 Nanoparticles to Enhance Photodynamic Therapy. *Adv. Funct. Mater.* **2016**, *26*, 5490−5498.
(56) Chuang, Y. T.; Cheng, T. Y.; Kao, T. L.; Liao, M. Y. Hollow AuxCu1-x Alloy Nanoshells for Surface-Enhanced Raman-Based Tracking of Bladder Cancer Cells Followed by Triggerable Secretion Removal. *ACS Appl. Nano Mater.* **2020**, *3*, 7888−7898.
(57) Mulvihill, M. J.; Ling, X. Y.; Henzie, J.; Yang, P. Anisotropic Etching of Silver Nanoparticles for Plasmonic Structures Capable of Single-Particle SERS. *J. Am. Chem. Soc.* **2010**, *132*, 268−274.
(58) Fateixa, S.; Correia, M. R.; Trindade, T. Resizing of Colloidal Gold Nanorods and Morphological Probing by SERS. *J. Phys. Chem. C* **2013**, *117*, 20343−20350.
(59) Phan-Quang, G. C.; Lee, H. K.; Phang, I. Y.; Ling, X. Y. Plasmonic Colloidosomes as Three-Dimensional SERS Platforms with Enhanced Surface Area for Multiphase Sub-Microliter Toxin Sensing. *Angew. Chem. Int. Edit.* **2015**, *54*, 9691−9695.
(60) Jacobson, R. H.; Zhang, X. J.; DuBose, R. F.; Matthews, B. W. Three-Dimensional Structure of Beta-Galactosidase from E. coli. *Nature* **1994**, *369*, 761−766.
(61) Marradi, M.; Chiodo, F.; Garcia, I.; Penadés, S. Glyconanoparticles as Multifunctional and Multimodal Carbohydrate Systems. *Chem. Soc. Rev.* **2013**, *42*, 4728−4745.

(62) Chen, J.; Alcaine, S. D.; Jiang, Z.; Rotello, V. M.; Nugen, S. R. Detection of Escherichia coli in Drinking Water Using T7 Bacteriophage-Conjugated Magnetic Probe. *Anal. Chem.* **2015**, *87*, 8977−8984.
(63) Chen, J.; Jackson, A. A.; Rotello, V. M.; Nugen, S. R. Colorimetric Detection of Escherichia coli Based on the Enzyme-Induced Metallization of Gold Nanorods. *Small* **2016**, *12*, 2469−2475.
(64) Ilarregui, J. M.; Kooij, G.; Rodríguez, E.; van der Pol, S. M. A.; Koning, N.; Kalay, H.; van der Horst, J. C.; van Vliet, S. J.; García-Vallejo, J. J.; de Vries, H. E.; van Kooyk, Y. Macrophage Galactose-Type Lectin (MGL) is Induced on M2 Microglia and Participates in the Resolution Phase of Autoimmune Neuroinflammation. *J. Neuroinflammation* **2019**, *16*, 130.
(65) Zhang, D.; Chen, Y.; Xu, X.; Xiang, H.; Shi, Y.; Gao, Y.; Wang, X.; Jiang, X.; Li, N.; Pan, J. Autophagy Inhibits the Mesenchymal Stem Cell Aging Induced by D-galactose Through ROS/JNK/p38 Signalling. *Clin. Exp. Pharmacol. Physiol.* **2020**, *47*, 466−477.
(66) Altschuler, S. J.; Wu, L. F. Cellular Heterogeneity: Do Differences Make a Difference? *Cell* **2010**, *141*, 559−563.
(67) Lawson, D. A.; Kessenbrock, K.; Davis, R. T.; Pervolarakis, N.; Werb, Z. Tumour Heterogeneity and Metastasis at Single-Cell Resolution. *Nat. Cell Biol.* **2018**, *20*, 1349−1360.
(68) Carter, B.; Zhao, K. The Epigenetic Basis of Cellular Heterogeneity. *Nat. Rev. Genet.* **2021**, *22*, 235−250.
(69) Lee, J. H.; Shin, H. J.; Kim, Y. D.; Lim, D. K. Real-Time Surface-Enhanced Raman Scattering-Based Live Cell Monitoring of the Changes in Mitochondrial Membrane Potential. *Nanoscale Adv.* **2021**, *3*, 3470−3480.
(70) Rice, M. E.; Harris, G. T. Comparing Effect Sizes in Follow-Up Studies: ROC Area, Cohen's d, and r. *Law Hum. Behav.* **2005**, *29*, 615−620.
(71) Le Ru, E. C.; Blackie, E.; Meyer, M.; Etchegoin, P. G. Surface Enhanced Raman Scattering Enhancement Factors: A Comprehensive Study. *J. Phys. Chem. C* **2007**, *111*, 13794−13803.
(72) Hsu, C. W.; Cheng, N. C.; Liao, M. Y.; Cheng, T. Y.; Chiu, Y. C. Development of Folic Acid-Conjugated and Methylene Blue-Adsorbed Au@TNA Nanoparticles for Enhanced Photodynamic Therapy of Bladder Cancer Cells. *Nanomaterials-Basel* **2020**, *10*, 1351.
(73) DeLong, E. R.; DeLong, D. M.; Clarke-Pearson, D. L. Comparing the Areas under Two or More Correlated Receiver Operating Characteristic Curves: a Nonparametric Approach. *Biometrics* **1988**, *44*, 837−845.
(74) Yang, Q.; Zhang, P.; Wu, R.; Lu, K.; Zhou, H. Identifying the Best Marker Combination in CEA, CA125, CY211, NSE, and SCC for Lung Cancer Screening by Combining ROC Curve and Logistic Regression Analyses: Is It Feasible? *Dis. Markers* **2018**, *2018*, 2082840.

https://doi.org/10.1021/acsami.1c13647
ACS Appl. Mater. Interfaces 2021, 13, 52295−52307